

**GT2011-45) +\***

## **IMBALANCE RESPONSE OF A ROTOR SUPPORTED BY HYBRID AIR FOIL BEARINGS**

**Daejong Kim**  
University of Texas at Arlington  
Arlington TX 76019, USA

**Prajwal Shetty**  
University of Texas at Arlington  
Arlington TX 76019, USA

**Donghyun Lee**  
Samsung Electro-Mechanics  
Suwon city, S. Korea

### **ABSTRACT**

Air foil bearings (AFB's) are widely used in small to midsized turbomachinery. They are simple in construction, offer very low drag friction, and have very high reliability at high speed operations. This paper presents experimental imbalance response of a 4.84 kg rigid rotor (operating below bending critical speed) supported by two hybrid air foil bearings with 50 mm in diameter. The concept of "hybrid" in this paper utilizes the hydrostatic augmentation of the load capacity during the start up and shut down. The hybrid air foil bearings were designed with three top foils for enhanced stability. Imbalance responses in cylindrical mode are presented up to 44,000rpm with different supply pressures. As the supply pressure is increased from 2.67 to 4 bar, the bearing stiffness increases slightly, resulting in slightly larger vibration (and reduced damping ratio) during the trans-critical speed operation. Hydrodynamic instability was observed with whirl frequency ratios of about 0.17~0.2 depending on the supply pressures. Tests were also conducted to investigate the effect of supply pressure on the rotordynamic stability. The test results show that the hybrid operation is very effective to suppress the subsynchronous vibrations at high speeds.

### **INTRODUCTION**

Air foil bearings have found many applications in small to midsized turbomachinery. A significant advantage of compliant foil journal bearings compared to conventional rigid surface bearings is their superior dynamic performance in rotor systems. Nowadays, many high speed turbomachinery implement air foil bearings in order to improve their mechanical efficiency. AFB's have greater reliability (when designed and installed properly) compared to rolling element

bearings as a result of reduced friction and oil free operation, consequently resulting in reduced scheduled maintenance.

For over three decades, air cycle machines for aircraft cabin pressurization use simple AFBs. AFBs used in Boeing 747 aircraft have demonstrated a robust service life with Mean Time Before Failure (MTBF) exceeding 100,000 hours [1]. Other applications include rotary flow compressor, micro-turbines [2] and oil-free turbochargers [3].

Foil bearings comprise of compliant smooth top foil which forms the bearing surface and corrugated bump foils which provides resilient support to the top foils. Coulomb-type damping exists in AFBs due to the relative motion between the bumps and the top foil, and between the bumps and the bearing housing.

Despite having a greater service life and reduced maintenance, AFBs have issues concerning dry rubbing during start/stop operations of the rotor. Top foils are coated with low friction solid lubricants such as Teflon in order to reduce the friction during the start/stops. Another drawback with AFB has been its heat dissipation capability. Parasitic heat energy developed due to viscous heating due to high speed operation is not easily dissipated. In addition, heat conducted from various parts of the machine can be too much for the air foil bearing to dissipate them effectively.

### **HYBRID AIR FOIL BEARING**

The term 'hybrid' is often used to denote foil-magnetic hybrid systems introduced in [11-13]. Foil-magnetic hybrid systems have been developed as foil bearing as a mechanical back-up bearing or as a main bearing at high speeds while magnetic bearing provides load support at start/stops. The technology has been developed since early 90's, and a few applications can be found in gas processing equipment.

The concept of hybrid air foil bearing (HAFB) in this paper is with hydrostatic augmentation combined with hydrodynamic foil bearing instead of the magnetic bearing.

Kim and Park [4] presented the first exploratory experimental work on HAFB made of simple compression springs as elastic foundation. Kumar and Kim [5] further developed the concept of the HAFB by applying the principle of HAFB to bump foil bearings, and presented a computational model to predict stiffness and damping coefficients of the HAFB. The study shows that HAFB has much smaller cross-coupled stiffness than hydrodynamic AFB in general, and these coefficients are strong function of orifice sizes, supply pressure, etc. Kumar and Kim [6] also presented experimental work on load capacity of the HAFB with bump foils with higher support stiffness. Low speed tests at 10,000 rpm for HAFB with 38.1mm diameter resulted in more than 150N load capacity with supply pressure of 4 bar. Both theoretical work in [5] and experimental works on HAFB [4] were on circular HAFB with continuous single top foil with four inherent restrictors.

Recently, Lee and Kim [7] presented large HAFB with size of 101.6 mm in diameter and 82.55 mm in length aiming for aero-propulsion application. The design was based on extensive rotordynamic analysis and parametric study to optimize the bump stiffness and top foil contour. The design is based on hydro-dynamically preloaded three-pad configuration with one hydrostatic orifice per each pad. They also extended the concept of the HAFB to thrust foil bearing [8] with novel radially-arranged bump foils for easy stiffness control and prediction. They present dynamic performance of the bearing from their computational model.

### Configuration of Three-Pad HAFB

The bearing discussed in this article has a three pad configuration as shown in Figure 1 with each pad having an arc angle of 120°. Each pad has its center offset from the global bearing center by a small distance,  $r_p$ . This type of configuration gives varying nominal clearance around the circumference of the bearing, with maximum clearance at the leading and trailing edges of the top foil and minimum set bore clearance,  $C_{SB}$ , at the center of the arc length of the top foil.

Non-dimensional hydrodynamic preload is defined as

$$R_p = 1 - \frac{C_{SB}}{r_p + C_{SB}} \quad (1)$$

The hydrodynamic preload is different from mechanical preload of the top foil generated by loose contact between the top foil and bump foils when the bearing is assembled onto the shaft.

### TEST RIG DESIGN

Figure 2 shows the photo of three-pad hybrid air foil bearing. Externally pressurized air is supplied to the bearing through three (3) orifice tubes attached to the backside of the top foil. The orifice tubes are located at three angular locations of 60°, 180° and 300°.

Figure 3 shows the cross section and photo of the test rig. A built-in 2-pole asynchronous motor with rated speed of 70,000 rpm drives the rotor supported by two HAFBs and hydrostatic air thrust bearing. The rotor has six UNC 2-56 threads on each side with each thread circumferentially offset by 60° for addition of calibrated imbalance. The bearing has 25µm thick Teflon coating on the SS 316 top foils, and the rotor has 5 µm thick dense Cr.

Table 1 summarizes the parameters of the bearing and rotor tested.

Table 1: Parameters of the test bearing

Rotor	Radius	24.5 mm
	Axial distance of imbalance locations	303 mm
	Mass	4.84 kg
	Translational moment of inertia	0.051 kgm <sup>2</sup>
	Polar moment of inertia	2.03×10 <sup>-3</sup> kgm <sup>2</sup>
	Bearing axial span	165 mm
	Probe axial distance	223 mm
HAFB	Length	37.5 mm
	Estimated radial set bore clearance	35 µm
	Design preload ( $r_p$ )	35 µm
	Design bump stiffness	14.45 GN/m <sup>3</sup>

### INSTRUMENTATION

Four eddy current type proximity probes measure the rotor vibrations as orthogonal pairs in two planes as shown in Figure 4. National Instruments PCI-4472 dynamic signal board (with 24-bit resolution, 102.4 kHz spontaneous sampling rate up to 8-channels) collects the data in the computer. Labview-based in-house rotordynamic software was developed for the measurements. The software has live-display monitoring capabilities of the time signal displays of the proximity probes and tachometer signal, XY plots of the rotor-center locus, rotor spin speed, and FFT frequencies of the time signals. Figure 5 shows a screen capture of the software while the rig is running. Post-processing programs written in MATLAB read the various saved files and performs several tasks, including: digital filtering the measured signals to extract the synchronous components, determine synchronous vibration amplitude and phase lag, and create waterfall plots of the FFT data.

The digital filter for the extraction of synchronous vibration is the 6<sup>th</sup> order Butterworth band-pass filter from MATLAB. All the test data were measured with 20kHz sampling frequency.

### RESULTS AND DISCUSSIONS

Imbalance response was measured at supply pressure<sup>1</sup> of 40 psi (2.67 bar) and 60 psi (4 bar) to the HAFBs. To measure

<sup>1</sup> All the supply pressures in the paper are gauge pressure.

the response to known amount of imbalance, small set screws were added at in-plane locations to generate calibrated imbalance of 3,800 mg-mm at each side of the rotor. Preliminary practice of baseline subtraction did not produce meaningful results due to the small difference of vibration magnitudes between the baseline and total signals (baseline + added imbalance). In addition, it was nearly impossible to match the speeds between the two tests (baseline and total) even if the motor is under speed control mode. Therefore, magnitudes and phase angles were found for the actual speeds the motor controller produces<sup>2</sup>, and they were used as reference values for cubic-spline interpolations of magnitudes and phase angles for the intended reference speeds. The cubic-spline interpolation was repeated five times (i.e., five test runs for both baseline and total) and they were used for final baseline subtraction.

Figure 6 presents one of the waterfall plots of the vertical signal from the responses of the rotor with 2.67 bar supply pressure. Speed increment is 250 rpm below 10,000rpm to detect the critical speed accurately, and then speed was increased with 1000rpm increment after 10,000rpm. Subsynchronous vibration of ~5,900 rpm begins to appear at around 20,000 rpm, but they are well-bounded until the speed reaches 30,000rpm. The baseline imbalance responses include the rotor static run-out and the residual rotor imbalance response, and they appear as large vibration (~10 $\mu$ m) all over the speed ranges. Waterfall plots of total response with added imbalances are presented in Figure 7. Figure 8 shows the baseline-subtracted synchronous imbalance response shown up to 15,000rpm. Large vibration along the horizontal direction is due to the stiffness anisotropy of the bearing due to the three-pad configuration. The phase angle curves for both horizontal and vertical vibrations are typical 2<sup>nd</sup> order behavior showing natural frequencies slightly lower than critical speeds. Natural frequency in horizontal direction of the cylindrical mode is at around 5,250 rpm, while natural frequency in vertical direction is around 7,200 rpm. The subsynchronous vibrations observed in Figure 6 and Figure 7 are close to the natural frequency in the horizontal direction.

Tests were repeated at 60 psi (4 bar) pressure. Waterfall plots of both baseline and total signals are shown in Figure 9 and Figure 10. As the pressure was increased, the bearing became more stable, allowing higher operating speeds with well-bounded limit cycles up to 34,000rpm. Large (but still smaller than at 30,000rpm with 2.67 bar) subsynchronous vibration appeared at 35,000rpm and similar limit cycle behavior continued until the maximum test speed of 44,000rpm.

Baseline-subtracted synchronous imbalance response is shown in Figure 11 up to 15,000rpm. Overall response is similar to the case of 2.67bar but vibration magnitudes at

---

<sup>2</sup> Actual speed is always slightly lower than the set speed in the controller because the drive motor is an induction type. In addition, slight fluctuation of the motor current and inverter frequency results in speed variations of about  $\pm 5$  rpm at low speeds and  $\pm 2$  rpm at high speeds.

critical speeds are slightly higher, which is due to the increased bearing stiffness (less damping ratio). Phase angles show similar behavior to Figure 8(b), and it is not presented.

To investigate the effect of supply pressure on the stability characteristics, the motor speed was set constant at 28,000rpm and supply pressure was varied from 40 psi (2.67 bar) to 70psi (4.67bar). Figure 12 compares the FFT plots of vertical signals at 28,000 rpm with different supply pressures. As the supply pressure is increased from 2.67 to 3.33 bar, subsynchronous vibration magnitude drops significantly from over 40 $\mu$ m to below 10 $\mu$ m. As the supply pressure is further increased to 4 bar, the subsynchronous vibration magnitude is further reduced to around 3 $\mu$ m. Further increase of the supply pressure to 4.67 bar reduces the vibration slightly but the difference is not significant. It is also noteworthy the subsynchronous frequency also slightly increases with supply pressure, i.e., ~5,900 rpm at 2.67 bar to ~6,500 rpm at 4.67bar, indicating slight increase of the bearing stiffness with the supply pressure. Figure 13 shows FFT plots at 29,000rpm with different pressures. Overall tendency is very similar to 28,000rpm. Figure 14 shows FFT plots at 30,000rpm with different pressures. Overall behavior is similar to the other two speeds but vibration magnitude at 3.33 bar is still large as much as nearly 30 $\mu$ m. Further increase of the supply pressure to 4 bar decreases the vibration down to the level below 10 $\mu$ m. Operation at speeds above 30,000rpm generated too large vibration when the supply pressure was below 3 bar. Therefore, minimum supply pressure for the tests at higher speeds was 3.33 bar. Figure 15 shows the results at 32,000rpm with different supply pressures. Initially the vibration magnitude was 27 $\mu$ m at 3.33 bar. As the supply pressure was increased to 4 bar, the vibration magnitude again dropped to below 10 $\mu$ m. Figure 16 shows FFT plots at 34,000 rpm with different supply pressures. Increasing the pressure to 4 bar decreased the vibration magnitude but the gain was small, and vibration magnitude was over 20 $\mu$ m at even the maximum supply pressure of 4.67 bar.

The test results show the hybrid operation is effective to suppress the subsynchronous vibrations up to 34,000rpm for the current bearing and rotor system.

## CONCLUSIONS

The test results clearly demonstrate the beneficial effect of the hybrid operation reducing the subsynchronous vibrations significantly up to 34,000rpm.

The test rotor is a solid long shaft with total weight of 4.84kg which is considered heavier than typical industrial applications supported by the similar-sized foil bearings. The bearing is expected to be stable above much high speeds than the maximum test speed in the paper when lighter rotor is used.

Further design optimization is necessary in the amount of hydrodynamic preload, assembly clearance, bump stiffness, etc, to increase the maximum operating speed.

**ACKNOWLEDGEMENT**

The test bearing was designed and built under the partial support of Texas Higher Education Coordinating Board under grant number 000512-0057-2007. The project was also partially supported by Korea Institute of Machinery and Materials.

**Bibliography**

- [1] Agrawal, G. L., 1997, "Foil Air/Gas Bearing Technology -- an Overview," International Gas Turbine & Aeroengine Congress & Exhibition, Orlando, FL, ASME Paper No. 97-GT-347.
- [2] Lubell, D., DellaCorte, C., and Stanford, M., 2006, "Test Evolution and Oil-Free Engine Experience of a High Temperature Foil Air Bearing Coating," Proceedings of the ASME Turbo Expo 2006, Power for Land, Sea and Air, Barcelona, Spain, May 8-11, ASME Paper No GT2006-90572.
- [3] Heshmat, H., Walton, J. F., DellaCorte, C., and Valco, M. J., 2000, "Oil Free Turbocharger Demonstration Paves Way to Gas Turbine Engine Applications," Turbo Expo 2000, ASME Paper No. 2000-GT-0620.
- [4] Kim, D., and Park, S., 2009, "Hydrostatic Air Foil Bearings: Analytical and Experimental Investigations," Elsevier Tribology International, **42**(3), pp. 413-425.
- [5] Kumar, M., and Kim, D., 2008, "Parametric Studies on Dynamic Performance of Hybrid Air Foil Bearings," Journal of Engineering for Gas Turbines and Power, **130**(6), pp. 062501-1-062501-7.
- [6] Kumar, M., and Kim, D., 2010, "Static Performance of Hydrostatic Air Bump Foil Bearing," Elsevier Tribology International, **43**(4), pp. 752-758, doi:10.1016/j.triboint.2009.10.015.
- [7] Kim, D., and Lee, D., 2010, "Design of Three-Pad Hybrid Air Foil Bearing and Experimental Investigation on Static Performance at Zero Running Speed," Journal of Engineering for Gas Turbine and Power, in Print.
- [8] Lee, D., and Kim, D., 2010, "Design and Performance Prediction of Hybrid Air Foil Thrust Bearings," ASME Journal of Engineering for Gas Turbines and Power, pp. In Print.
- [9] Rimpel, A.M., 2008, *ANALYSIS OF FLEXURE PIVOT TILTING PAD GAS BEARINGS WITH DIFFERENT DAMPER CONFIGURATIONS*, Texas A&M University.

**List of Figures**

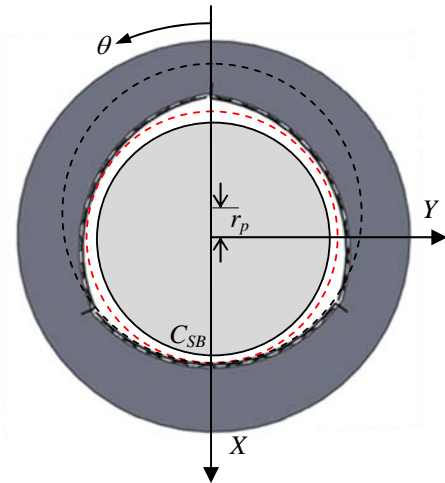


Figure 1 Schematic of a HAFB showing preload, set bore clearance and pad configuration

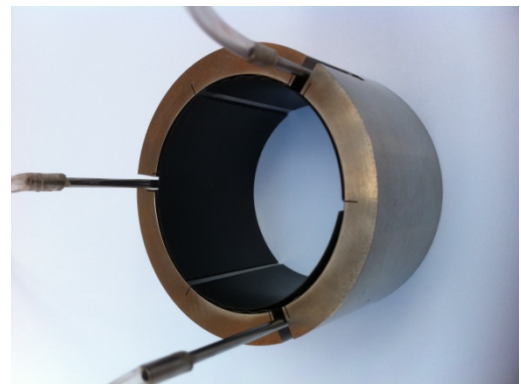
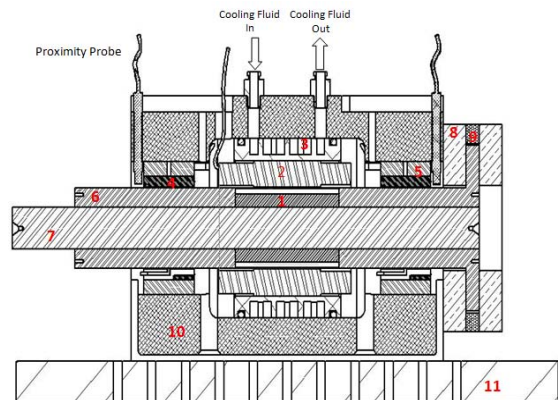
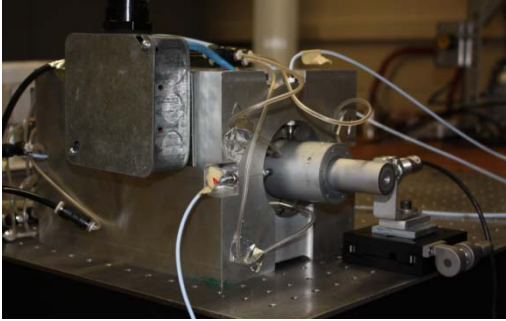


Figure 2 Photo of the hybrid air foil bearing



(a) Cross-section view of the test rig



(b) Photo of the test rig

Figure 3 Cross-section view and photo of the test rig

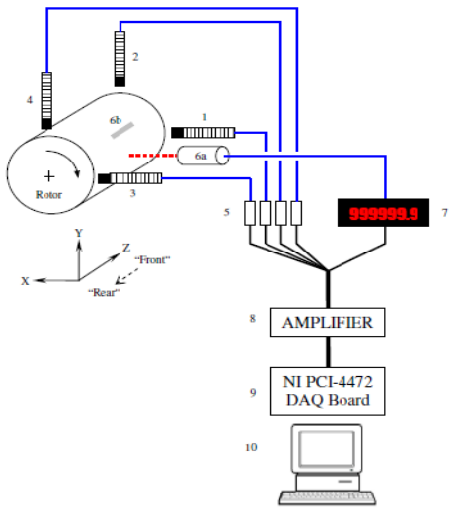


Figure 4: Layout of the data acquisition system, image from [9]

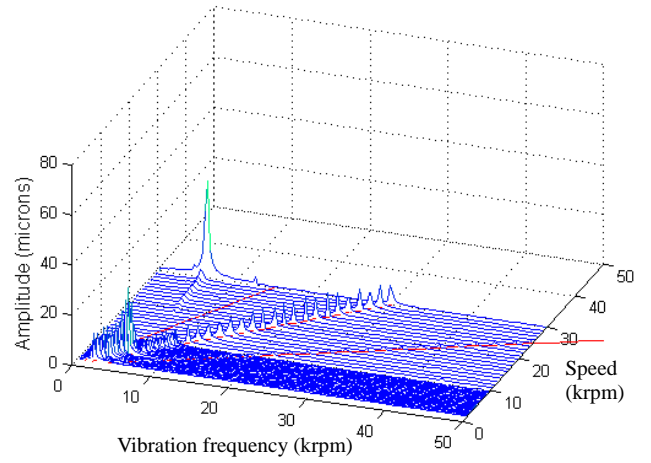


Figure 6 Waterfall plot of baseline signals in vertical direction, 2.67 bar supply pressure

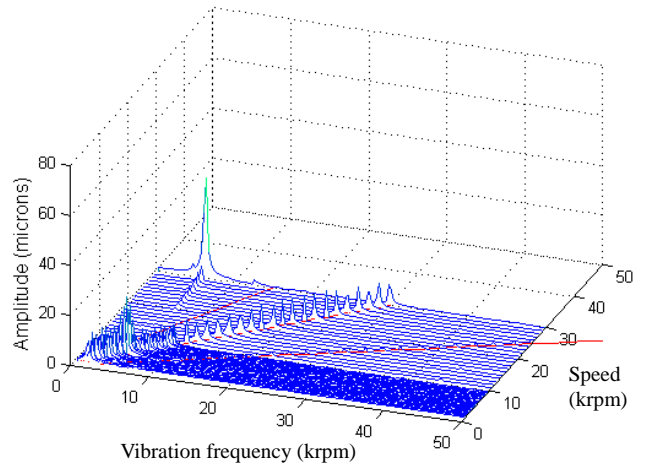
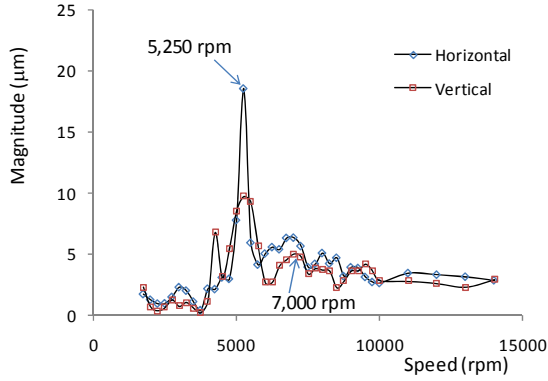


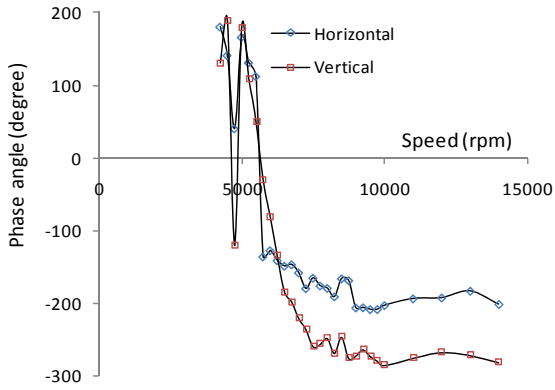
Figure 7 Waterfall plot of total signal in vertical direction with added imbalance, 2.67 bar supply pressure



Figure 5 Screen capture of Labview-based in-house rotordynamic software



(a) Magnitude plot



(b) Phase plot

Figure 8 Calibrated imbalance responses with in-phase imbalance, 2.67 bar supply pressure

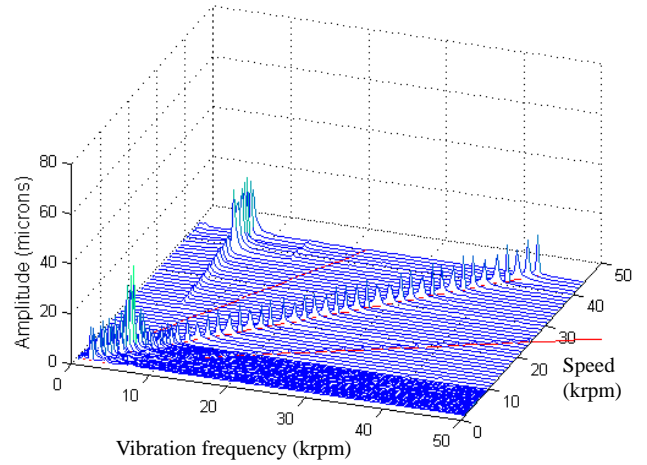


Figure 9 Waterfall plot of baseline signal in vertical direction, 4 bar supply pressure

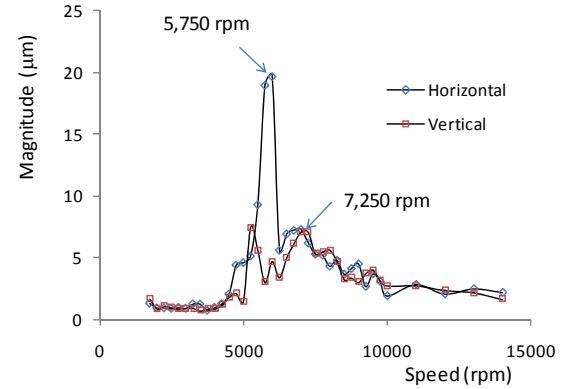


Figure 10 Waterfall plot of total signal in vertical direction with added imbalance, 4 bar supply pressure

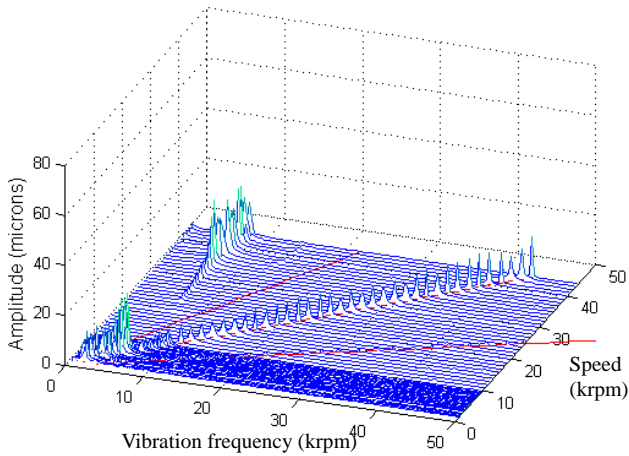


Figure 11 Calibrated imbalance responses with in-phase imbalance, 4 bar supply pressure

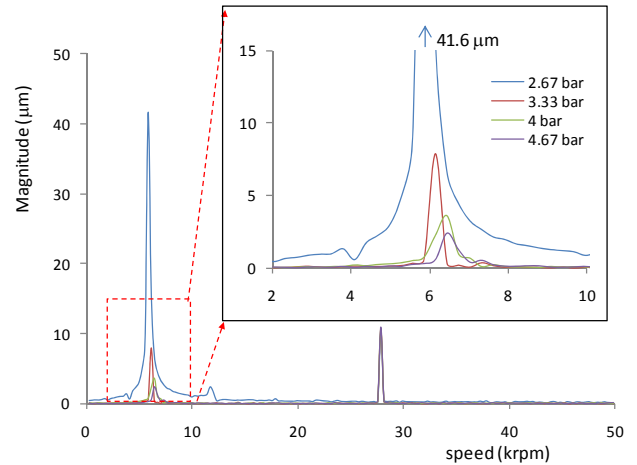


Figure 12 FFT of vertical signals at 28,000 rpm with different supply pressures

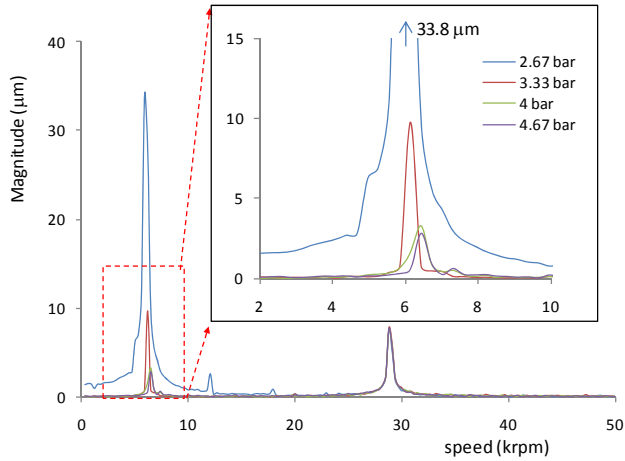


Figure 13 FFT of vertical signals at 29,000 rpm with different supply pressures

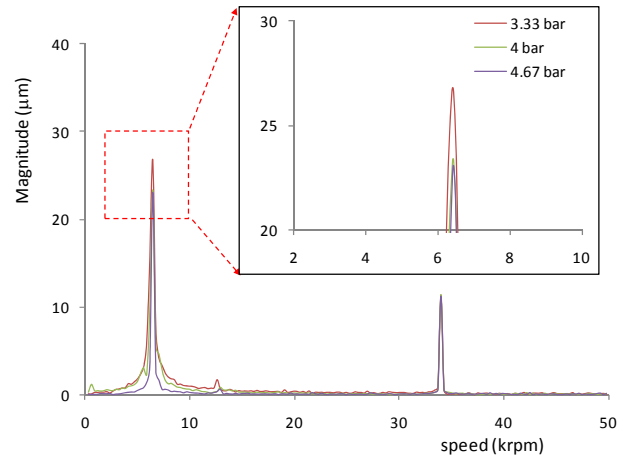


Figure 16 FFT of vertical signals at 34,000 rpm with different supply pressures, magnitude in peak-to-peak

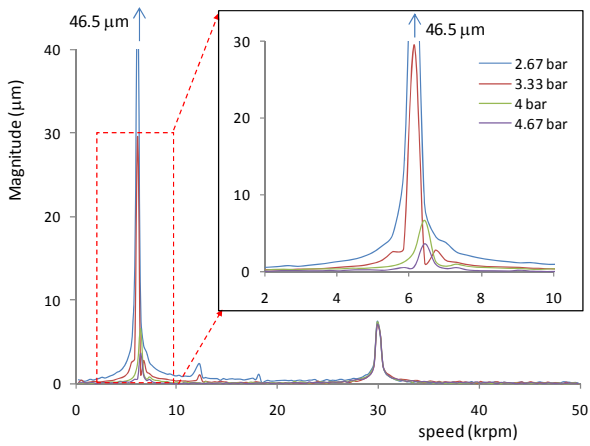


Figure 14 FFT of vertical signals at 30,000 rpm with different supply pressures

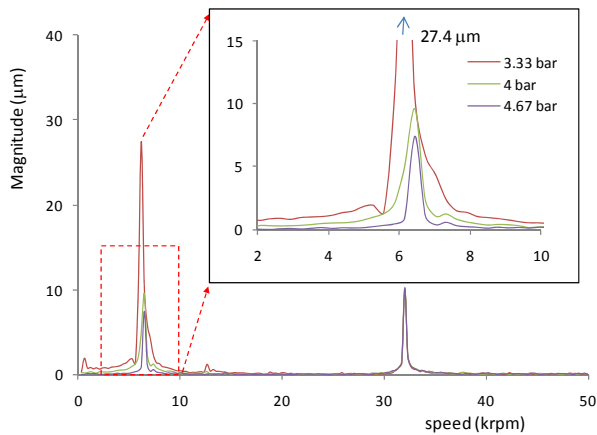


Figure 15 FFT of vertical signals at 32,000 rpm with different supply pressures